Characterization of Pt and Ir oxyhydrate surface layers from anodized, polycrystalline Pt and Ir Foils

Benjamin Johnson, Chinmoy Ranjan, Mark Greiner, Rosa Arrigo, Manfred Schuster, Britta Höpfner, Mihaela Gorgoi, Iver Lauermann, Marc Willinger, Axel Knop-Gericke, Robert Schlögl

Abstract

Pt and Ir polycrystalline foils have been electrochemically oxidized through anodization to create thin platinum and iridium hydrous oxide layers and are analyzed with laboratory photoelectron spectroscopy during heating and time series (temperature programmed spectroscopy). The films contain oxygen in the form of a bound oxide, water and hydroxides which are investigated by depth profiling with high energy photoelectron spectroscopy. The Pt films are unstable and begin to degrade immediately after removal from the electrolyte, forming a core-shell structure with a metallic inner core and a hydrous oxide outer shell almost devoid of Pt. However, evidence of meta-stable intermediate states of degradation is found, which offer possibilities for manufacturing PtO_x phases with increased stability. Heating the film to even 100°C causes accelerated degradation and shows that stoichiometric oxides such as PtO_2 or PtO are not the active species in the electrolyte. The Ir films exhibit increased stability and higher surface Ir content and gentle heating at low temperatures leads to a decrease in defect density. Although both layers are based on noble metals, their surface structures are markedly different. The complexity of such hydrous oxide systems is discussed in detail with the goal of identifying film composition more precisely.

1. Introduction

Establishing new, alternative sources of energy is currently the topic of intense research around the world. Moving away from fossil fuels will lead to a multifaceted energy economy based on several kinds of renewable sources such as wind, solar and wave/tidal: technologies,

which have already made an impact on the world energy market.

One promising solution is the production of hydrogen through water splitting by electro-oxidation of oxygen in water. Common to all photochemical harvesting methods, this process is also found in living plants where oxygen and hydrogen are split via photosynthesis when light is absorbed in a leaf and charge (core-hole) separation occurs. The holes lead to the oxidation of water and production of oxygen by the oxygen evolving complex (OEC) in photosystem II with byproducts of electrons and protons. These then enter photosystem I and produce hydrogen in the form of NADPH through a ferrodoxin-$NADP^+$ reductase. Guided by the photosynthesis processes in plants, Daniel Nocera explores these ideas with his well-known artificial leaf in the form of a solid state, wireless cell [1]. Here a triple junction Si solar cell is sandwiched between an artificial OEC, self-assembled from cobalt, oxygen and phosphate and a hydrogen-evolving NiMoZn catalyst. As in photosystem II, the Co-OEC oxidizes water through a four-electron transfer mechanism. However, in contrast to nature, which has developed healing mechanisms for its components, catalysts under real working conditions (open-flow systems) must exhibit high stability, especially during the oxygen evolution reaction because they cannot self-heal. We note also that we do not consider re-precipitation to be a viable repair strategy [2].

Therefore, materials science attempts to develop not only efficient, but also stable catalysts. Basic models of these assume simple oxides such as TiO_2 and perovskite structures such as RuO_2 and IrO_2, but do not consider the role of water in the catalyst structure. Further work requires not only identifying new materials, but also an understanding of the standard active catalysts themselves in terms of structure, chemical reactivity and electron transport, most notably PtO_x and IrO_x [3]-[13].

Although the actual goal is hydrogen generation, this reaction is dependent on a simultaneous oxygen evolution reaction (OER), which is the limiting factor in real systems. Research into this process hinges on understanding the mechanistic complexity of the 4-electron transfer and the corrosive nature of the OER, which makes manufacturing suitable catalyst

materials challenging [14]. In this study we contribute to this task by analyzing the true active nature of OER catalyst systems using photoelectron spectroscopy to obtain compositional data of the active materials PtO_x and IrO_x.

When grown anodically from precursor metallic foils, the result is a highly complex hydrous oxide film which has often been studied for both anodic oxygen evolution and cathodic hydrogen evolution. However, especially in terms of layer composition, many of the studies rely on simplified models in order to arrive at descriptions of the synthesized films. While a promising first step, more detailed studies must be completed to further refine our understanding. An exact knowledge of film composition is a prerequisite to understanding the electronic dynamics through the layers and the interaction between oxygen and the catalyst at the active sites.

Here we attempt through several different X-ray photoelectron spectroscopic (XPS) methods to illuminate the complexities of the Pt and Ir systems resulting from anodization. This includes high-energy photoelectron spectroscopy (XPS) data for new insight into the depth profiles of such films and heightened scrutiny of standard XPS data to extend our understanding beyond the usual interpretation. Expanding on our past studies [15, 16, 17] we combine XPS results with scanning electron microscopy to successfully examine the relationship between morphology and electronic structure in these complex layers.

2. Experimental

Both the platinum and iridium bulk hydrous oxide layers were formed by anodization of polycrystalline Pt and Ir metal foils, respectively. Polycrystalline foils are rich in defects, for example at grain boundaries, and can be oxidized more easily than single crystals.

The Pt samples were synthesized in 0.5 M H_2SO_4 at 2.5 V vs. reversible hydrogen electrode (RHE) while evolving oxygen. Under these conditions both Pt oxidation and oxygen evolution are significantly accelerated and the result is the growth of a pale brown film on

the foil surface. The duration of synthesis varied between one and two hours according to the desired film thickness. Subsequent handling in air is unlikely to have had an oxidizing effect on the foil because the preparation was under extremely oxidizing conditions. However, turning off the applied potential may have resulted in chemical reduction.

The Ir samples were synthesized at room temperature under acidic conditions while cycling between 0 and 1.5 V vs. RHE. Known to be electrochromic, the Ir samples were removed from the electrolyte at 0 V vs. RHE (bleached). For the laboratory XPS measurements the sample was grown for 120 cycles, removed from the electrochemical cell and measured in the XPS chamber after differing durations in air (see Results and Discussion).

The resulting Pt and Ir samples were formed largely from bulk hydrous oxides of ill-defined stoichiometry and we have chosen the nomenclature $MO_x(OH)_y(H_2O)_z$, with M the metal component Pt or Ir, to describe them. The formula explicitly portrays the complexity of the films and leaves the stoichiometry in general terms. The subscripts x, y and z in both Pt and Ir samples are not meant to denote any similarities in the respective stoichiometries and are chosen for convenience.

The laboratory XPS chamber used here has a base pressure of $\sim$8x10^{-10} mbar and is equipped with a Phoibos 150 MCD-9 hemispherical electron analyzer from Specs GmbH. Measurements were calibrated with Au $4f_{7/2}$ at 84.0 eV and Cu $2p_{3/2}$ at 932.7 eV. The high kinetic energy measurements were performed on the HIgh Kinetic Energy (HIKE) end station at the KMC-1 beamline at the Electron Storage Ring BESSY II at the Helmholtz Zentrum Berlin für Materialien und Energie in Berlin, Germany using the Si (111) monochromator crystal and a SCIENTA R4000 high-resolution hemispherical electron anlayzer with a resolution of $\sim$1.1 eV [19]. Quantitative XPS results were achieved by normalizing the fitted XP peaks with the number of scans, ionization cross-sections (taken from [20] for laboratory measurements and from [21] for HIKE measurements) and, in the case of the laboratory measurements, the transmission function of the electron analyzer. The mean free path of

the photoelectrons was also taken into consideration although this quantity is strongly dependent on the unknown stoichiometry of the sample.

3. Results and Discussion

4. $PtO_x(OH)_y(H_2O)_z$

Fig. 1 a) shows a typical XP survey spectrum (Mg Kα) of a $PtO_x(OH)_y(H_2O)_z$ bulk hydrous oxide film from an anodized polycrystalline Pt foil. Pt and O lines are evident along with S and N in small amounts from the synthesis process. b) shows a detail of the Pt 4f state measured with Mg Kα with the associated Pt 1 (often denoted Pt^0 or metal in the literature), Pt 3 (often denoted Pt^{2+}) and Pt 4 (often denoted Pt^{4+}) peaks, where we continue our nomenclature from Arrigo, *et al.* [15]. The fit parameters used are given in table 1 and show the quality of the fit: the peak binding energies and spin orbit splitting, ΔE, between the $4f_{5/2}$ and $4f_{7/2}$ components were fixed only for Pt 1 with the binding energy and ΔE of the Pt 3 and Pt 4 components allowed to vary. The table shows all three ΔE values to be similar as expected.

We observed the Pt 1 peak within an hour of synthesis on layers tens of nm thick, meaning the Pt 1 (metal) signal does not originate from the metal substrate. Therefore, we infer the degradation of the oxidized foil to metal (Pt 3/4 $\rightarrow$ Pt 1) begins soon after the completion of synthesis, although it has not been determined at which stage the degradation begins. At the time of the measurement the atomic [Pt]/[O] ratio was 0.14 and will be discussed later with the HIKE results.

A more detailed look at the impurities in the thin layers in figure 1 c) shows the S 2p measurement with peaks at 168.1 eV and 169.4 eV, indicating S present as thiosulfate and sulfate, respectively, while 1 d) shows the N 1s measurement with peaks at 401 eV and

399.2 eV indicating N present in the form of N-O and C-N-H compounds.

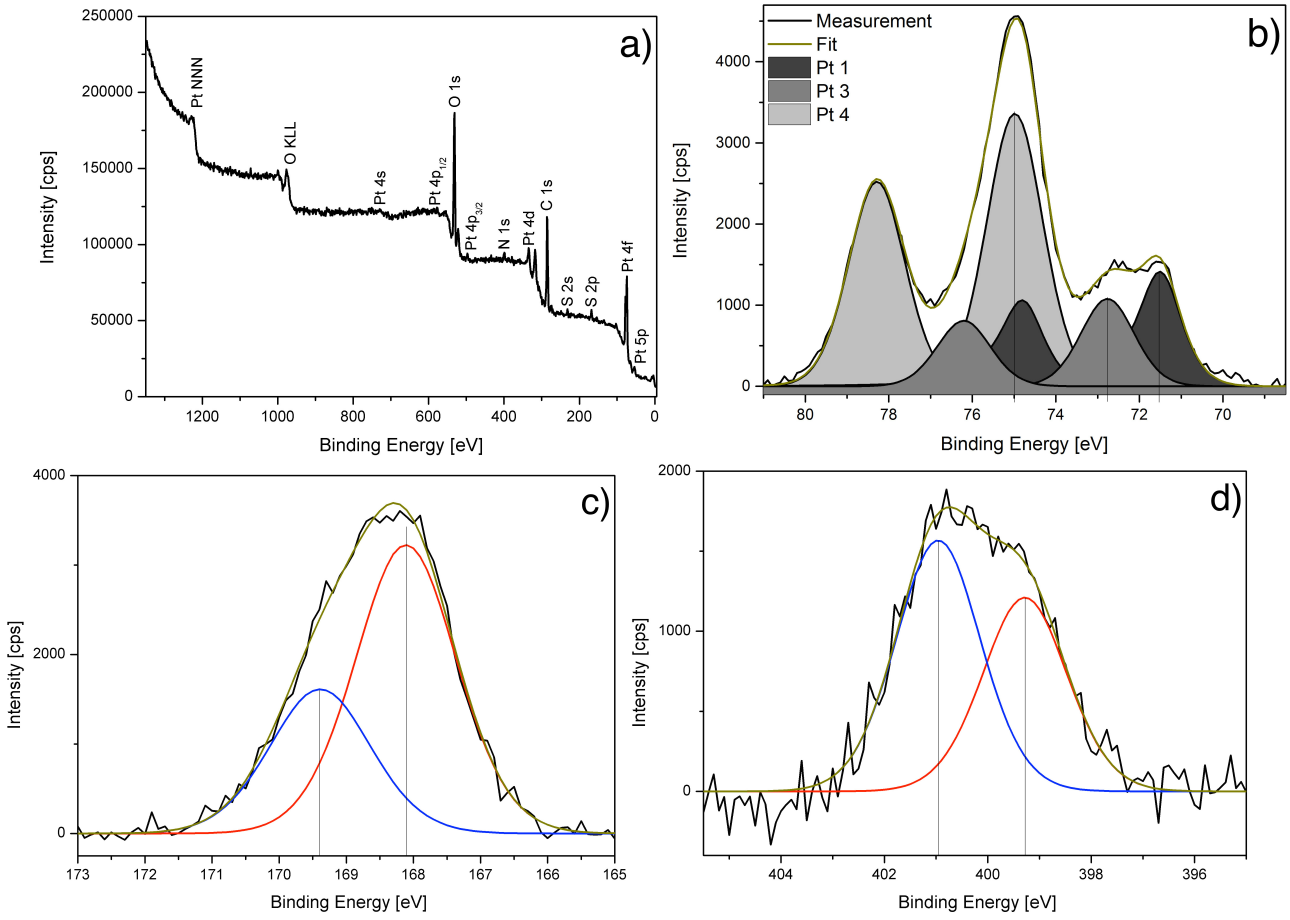

FIGURE 1. a) Typical XP survey spectrum of $PtO_xOH_y(H_2O)_z$ showing the constituent elements of Pt, O, S and N. b) typical detail of Pt 4f (Mg Kα). Three peaks, Pt 1, Pt 3, Pt 4, are marked and correspond to the common literature nomenclature Pt^0 (metal), Pt^{2+} and and Pt^{4+}, respectively. The atomic [Pt]/[O] ratio was 0.14. c) S 2p spectrum showing contributions at 168.1 eV and 169.4 eV which indicate the presence of thiosulfate ($S_2O_3^{2-}$) and sulfate (SO_4^{2-}) species. d) N 1s spectrum showing contributions at 401 eV and 399.2 eV indicating the presence of N-O and C-N-H species. The traces of S and N are left from the synthesis process.

The Pt 1 signal in fig. 1 b) is due to layer degradation (oxide reduced to metal) found in thin layers and not from exposure to the X-ray source (beam damage). Such a test was necessary because beam damage has been observed elsewhere, albeit under near-ambient conditions [22]. Pt 4f photoelectron spectrum from a thick sample (~200 nm) prepared with the same synthesis found in the previous section but with a longer five hour anodization time is displayed in fig. 2. The longer oxidation time creates a surface PtO_2 layer with

no Pt 1 (metal) component in XPS showing the sample to be stable during exposure to X-rays. The thicker sample is, however, unsuitable for further catalytic study because the surface layers have no direct contact to the oxide-metal foil interface and charge transport is reduced. Further experiments were performed on thinner Pt oxide layers.

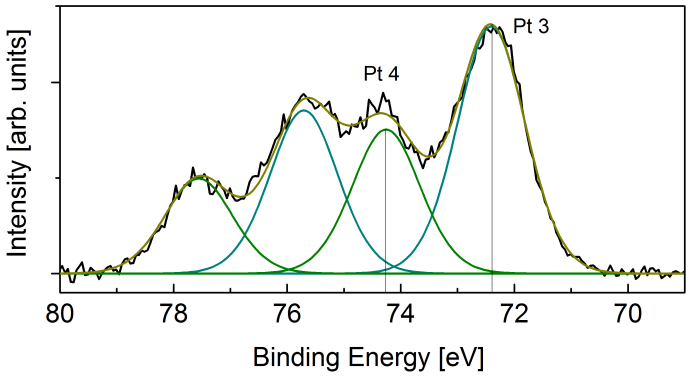

FIGURE 2. Pt 4f XP spectrum from a thick (∼200 nm) PtO_2 sample. The absence of a Pt 1 (metal) peak shows the stability of the oxide layer during exposure to X-rays. The presence of the Pt 1 peak in the thinner layers is due to layer degradation and not the result of beam damage.

TABLE 1. Parameters for the Pt 4f XPS fits. The line shape in pro cent Gauss (G) and Lorentz (L) and possible asymmetry parameter (AS), binding energy (B.E.) of the Pt $4f_{7/2}$ component, full width at half maximum (the same for the Pt $4f_{7/2}$ and Pt $4f_{5/2}$ components) and peak separation, ΔE, between 7/2 and 5/2 components are given.

	Pt 4	Pt 3	Pt 1
Line Shape	40% G, 60% L	40% G, 60% L	40% G, 60% L + AS
B.E. ($4f_{7/2}$)	74.67 eV	72.34 eV	71.19 eV
FWHM	1.55 eV	1.71 eV	1.08 eV
ΔE	3.31 eV	3.32 eV	3.30 eV

As a reference for the nomenclature found in the literature for both the Pt and Ir systems, table 2 contains often-cited publications with original discussions of Pt and Ir oxide films as well as several more current studies. Publications containing measurements sensitive to actual long-range order, for example EXAFS, are less common, although some can be found [23]. Considering the O 1s peak in fig. 3 and that our method of synthesis lacks any thermal treatment, we hesitate to use the literature nomenclature, as the present system is surely of greater complexity than these labels reveal (perhaps even for the metal state). The O 1s

signal contains contributions at the usual binding energies quoted for oxygen bound into an oxide phase (530 eV), hydroxides (531.8 eV) and H_2O (533.1 eV). The largest contribution appears at energies near OH^- [24, 25, 26] with a low intensity at 530 eV showing only a small amount of the oxygen is in oxide form. A possible method of full peak analysis can be found in [15] and resulted here in the stoichiometry $PtO_{0.09}(OH)_{6.4}(H_2O)_{0.86}$ after taking the carbon-oxygen bond contributions into account. We consider, therefore, the Pt (or Ir) atoms to be bound in an array of different local environments causing a broadening of the O 1s peak and 4f constituent signals grouped into the Pt 1, Pt 3 and Pt 4 peaks in fig. 1.

TABLE 2. Examples of current and past literature using common nomenclature with well-defined oxidation states in the PtO_x and IrO_x systems. "Basis" refers to the reasons for the chosen nomenclature in each study. For specific oxidation states and binding energies, please refer to the original article.

Publication	Year	System	Basis	Comments
W.N. Delgass, *et al.* [27]	1971	Pt, powder	Reference Materials	Does not contain anodized films
K.S. Kim, *et al.* [28]	1971	Pt, foil	Reference Materials	
G.C. Allen, *et al.* [29]	1974	Pt, foil	Literature Values	Uses "Oxide I" and "Oxide II" but discusses mainly Pt^{2+} or Pt^{4+} as possibilities. Discusses mixed $Pt(OH)+Pt(OH)_2$
J.S. Hammond, *et al.* [30]	1977	Pt, foil, polycr. plug	Literature Values	Uses "Oxide I" and "Oxide II" but discusses only Pt^{2+} or Pt^{4+} as possibilites. Cites controversy in literature.
M. Salmerón, *et al.* [31]	1981	Pt, Ir Single Crystals		Uses LEED, AES to discuss proposed unit cell.
M. Peuckert, *et al.*[32]	1984	Pt, (111)	Reference Materials	
M. Peuckert [33]	1984	Ir, (111)	Reference Materials	Discusses only IrO_2 as possibility
J.B. Goodenough, *et al.* [34]	1988	Pt, powder	Literature Values	
L. Atanasoska, *et al.* [35]	1990	Ir, thermal decomp.	Literature Values	Discusses disagreement in literature
G. Lalande, *et al.* [36]	1999	Pt-Ru, powder	Literature Values	
B. Yang, *et al.* [37]	2003	Pt -Ru-C, powder	Literature Values	
R. Arrigo, *et al.* [15]	2013	Pt metal	New Nomenclature	This nomenclature is used in the current study
S. Axnanda, *et al.* [38]	2015	Pt/Liquid Junction	Literature Values	

Further investigation on the stability and "oxide"-nature of the anodized layer was performed through a series of measurements with the sample subjected to temperature programmed XPS via electron beam heating from the backside of the sample.

Fig. 4 shows rapidly measured Pt 4f spectra recorded at the indicated temperatures with two different peak fit series found in fig. 5. The reduction of the Pt 4 peak at 78 eV shows the film begins to rapidly degrade at less than 100°C and proceeds through many intermediate

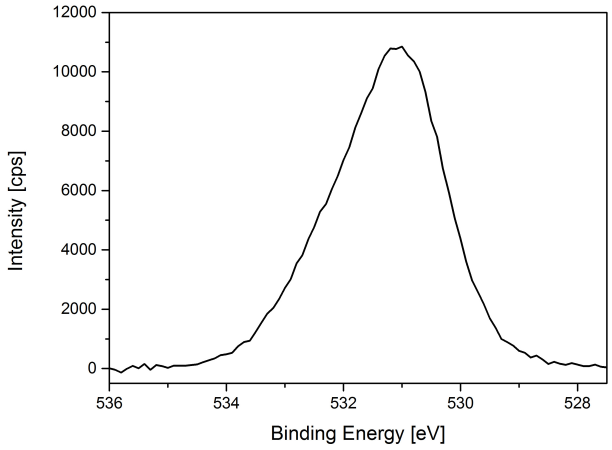

FIGURE 3. Detail of O 1s peak from the $PtO_x(OH)_y(H_2O)_z$ anodized film. Contributions to the spectrum can be found at binding energies 530 eV, 531.8 eV, 533.1 eV corresponding to oxygen bound into an oxide, hydroxides and H_2O, respectively. The small contribution at 530 eV shows most of the oxygen is not in oxide form.

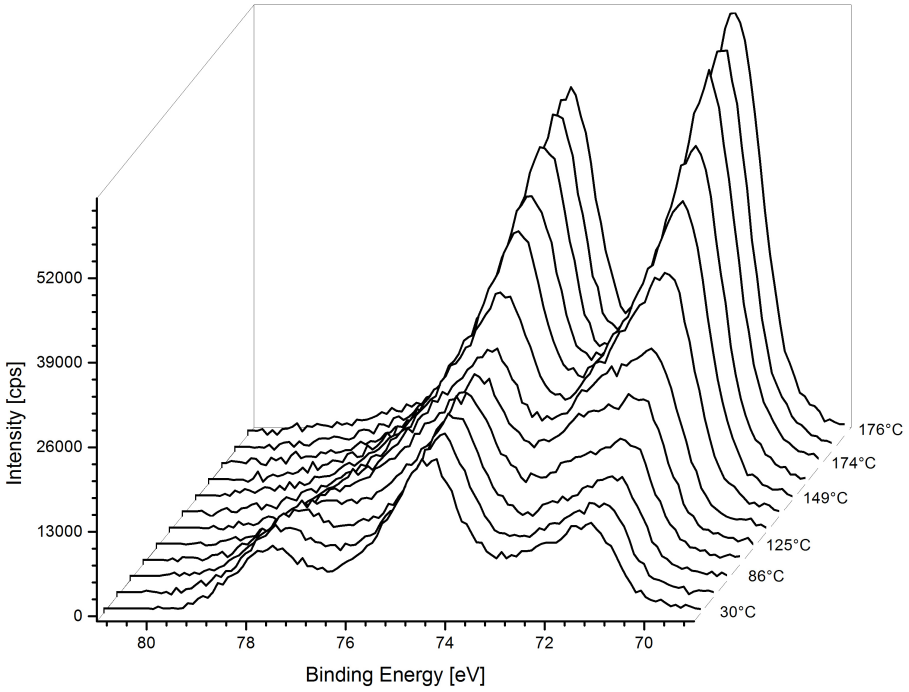

FIGURE 4. Heating series of $PtO_x(OH)_y(H_2O)_z$: rapidly measured Pt 4f detail spectra taken at the indicated temperatures. The change in signal intensity is indicative of the transition toward metal and shows explicitly intermediate thermodynamic states. The degradation seen at low temperatures shows the initial material is not a stoichiometric oxide phase such as PtO or PtO_2.

states of undetermined stability. For stoichiometric PtO_2 films we would expect stability to $\sim$200°C and even higher temperatures for PtO [41]. The degradation at the low temperature

in fig. 4 shows the original film cannot be a stoichiometric oxide structure like PtO_2 or PtO. Furthermore, the sample has no defined temperature of decomposition as the component signals in fig. 4 change at different temperatures over intervals of minutes. However, we have not determined whether the observed change is due to increased diffusion during heating or sample degradation.

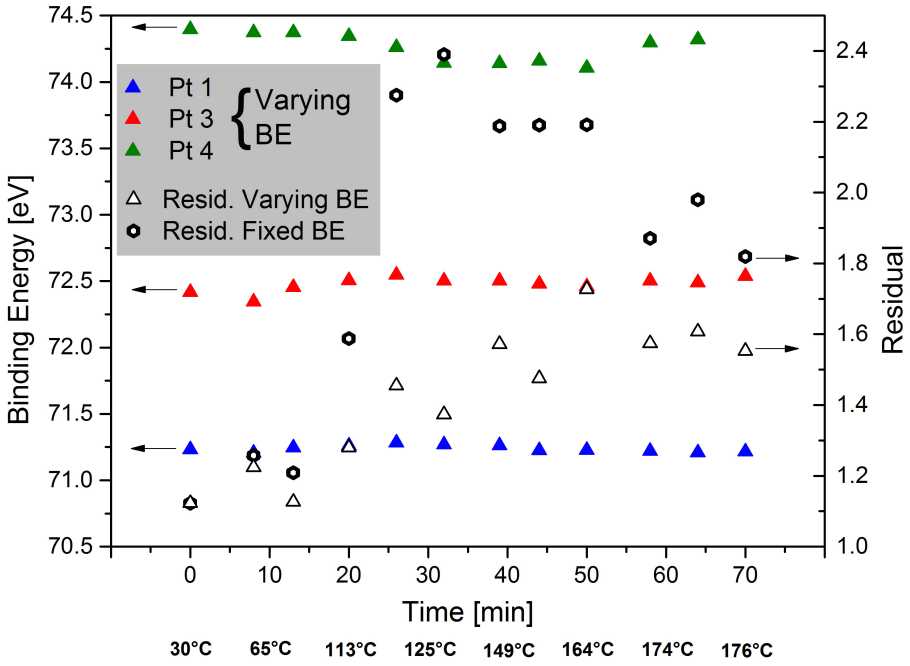

FIGURE 5. Fit series of the spectra from fig. 4. The first series (colored triangles) uses the fit parameters from the spectrum at time $t = 0$ and 30°C to fit the remaining spectra. Only the binding energies of the Pt 1, Pt 3 and Pt 4 doublets were allowed to change and are plotted along with the resulting fit residual (open triangles). In the second series only the residual (open hexagons) is shown. Here all parameters from the initial spectrum were held constant for the subsequent spectra and the need for additional components between 150°C and 160°C is evident.

For the fit series in fig. 5, the initial fit parameters were taken from the spectrum at time $t = 0$ and 30°C and are

Deviations from the values in table 1 may be attributed to the low signal-to-noise ratio of the initial spectrum (only one sweep) and that the sample here is from a different synthesis run. Especially the lower Pt 4 intensity contributes to an uncertainty in the binding energy

TABLE 3

	Pt 4	Pt 3	Pt 1
Line Shape	40% G, 60% L	40% G, 60% L	40% G, 60% L + AS
B.E. ($4f_{7/2}$)	74.40 eV	72.42 eV	71.23 eV
FWHM	1.65 eV	1.65 eV	1.27 eV
ΔE	3.30 eV	3.30 eV	3.30 eV

of this component.

In the first fit series (colored triangles), the initial parameters in table 3 were fixed except for the binding energy of the doublet pairs (ΔE was also fixed). The variation in binding energy is displayed along with the residual of the fit (open triangles) in fig. 5. In the second series (open hexagons) all parameters from the initial fit were fixed and only the residual is shown. Although the initial fits are satisfactory in both cases, the residual begins to increase at ~30 min with the maximum in both series coinciding with the maximum shift of the Pt 4 peak away from its initial position. Both maximum residuals in fig. 5 then begin to decline and would presumably return to low values if the system had been completely reduced to metal. In order to improve the fits between 30 min and 55 min, another peak doublet is needed and indicates a new species present during degradation. A doublet with a $4f_{7/2}$ binding energy 0.6 eV higher than Pt 1 appears in literature in our past studies [15] and is assigned to chemisorbed oxygen on a single crystal in [22]. However, adding a peak at this binding energy did not improve the fit; the best results were achieved with a doublet with a $4f_{7/2}$ binding energy of 73.5 eV. This energy is between that of Pt 3 and Pt 4 and would correspond to an oxidation state of approximately 3+, assuming it is an electrically well-contacted compound and can be referenced to E_f. However, although evidence for such intermediate species exists (see again [15]) we stop short of any such concrete interpretation on the basis of XPS data alone.

Further valence band measurements before and after heating are shown in fig. 6 a) along with the O 1s spectrum showing the expected decrease in oxygen signal intensity. The shift of the d-band and emergence of a Fermi Level underscores the appearance of the metallic

phase after sample degradation [33, 39] although fig. 6 b) shows the surface of the sample was not completely reduced by heating in the vacuum. A clean Pt-metal reference using asymmetric peaks (not shown) was used to determine the exact form of the bare metal signal and is not sufficient here to fit the final state after heating in fig 6 b); additional peaks are needed to represent the remaining Pt 3 phase. This is more stable than the Pt 4 phase and leads, after heating, to a sample surface with a patchwork of Pt 1 and Pt 3 regions and shows the lateral inhomogeneity on the scale of the XPS measurement spot ($\sim$1 mm^2). The main initial degradation pathway here is Pt 4 $\rightarrow$ Pt 3 $\rightarrow$ Pt 1 with the initial growth of the Pt 3 signal relative to Pt 1. After about thirty minutes this behavior reversed and the growth of the Pt 1 signal dominated. An overall comparison of before and after heating shows a reduction in oxygen and carbon relative to platinum. The Pt : O : C was 1 : 5.3 : 9.7 before and 1 : 1 : 2.5 after heating. We also note that despite the low expected conductivity of the material, the steady signals obtained in fig. 4 indicate no differential charging of the sample.

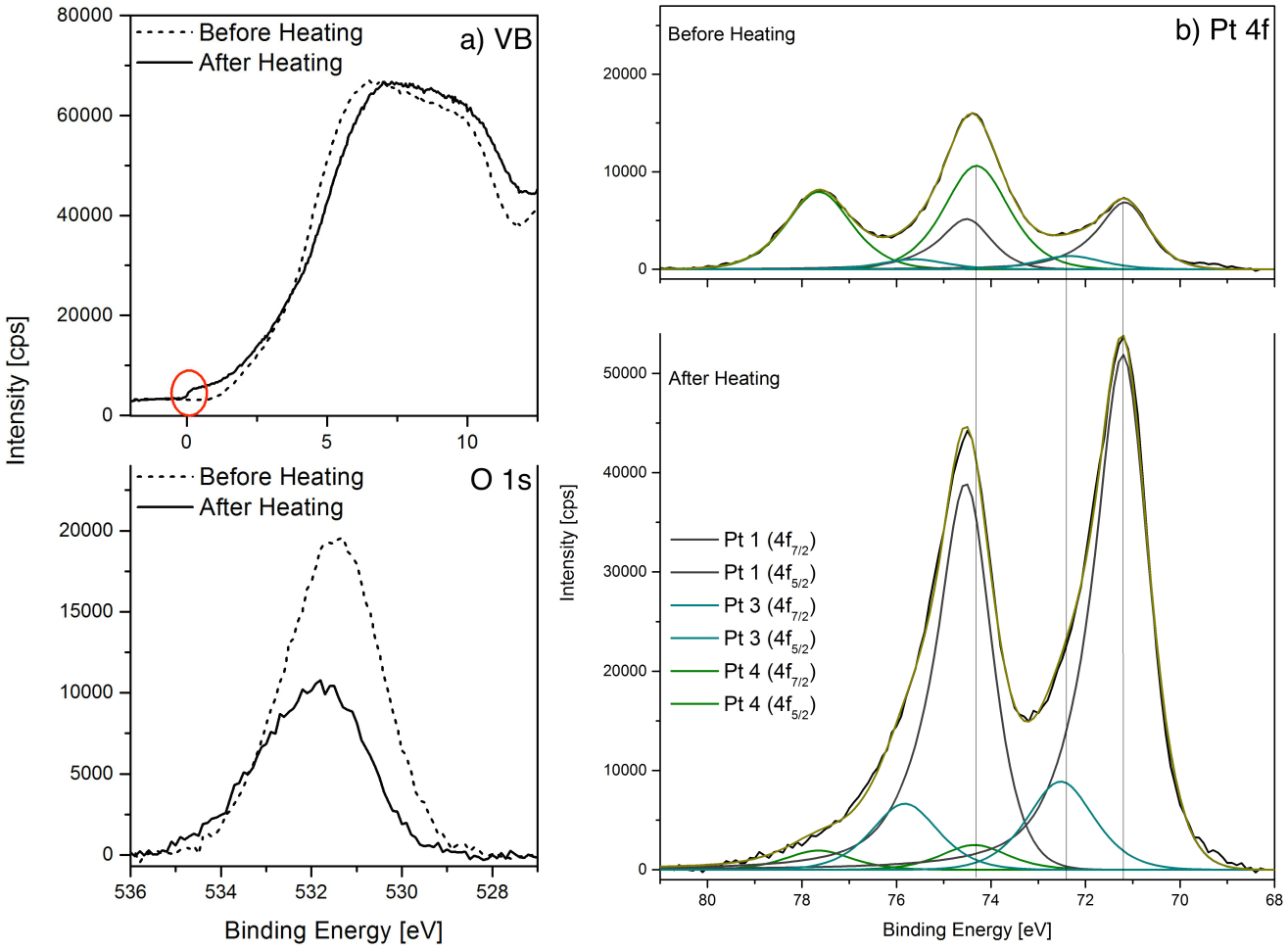

FIGURE 6. a) He I valence band and O 1s spectra before and after heating of $PtO_x(OH)_y(H_2O)_z$ to 176°C during which the Fermi Level clearly emerges. b) compares the Pt 4f detail spectra before and after heating. The change in peak form is indicative of the transition toward metal through intermediate states.

The investigation continued with experiments using a time series. Here, different pieces (labeled 'a' through 'g') of an anodized Pt foil strip 5 mm × 20 mm were observed after differing times in air and in vacuum (fig. 7). "As Introduced" denotes samples introduced into the vacuum after being in air for the indicated time after synthesis and "Next Day" denotes the same sample after remaining in vacuum for an additional time after the "As Introduced" measurement was completed. Fig. 7 a) and b) show the Pt 4f detail spectra from samples 'a' and 'f,' which are extreme samples – soon after synthesis and after an extended time in air, respectively (peaks have not been normalized). It is evident that the degradation follows the pathway in which most of the Pt 4 is reduced to Pt 3 while much smaller amounts of Pt 4 and Pt 3 are reduced to Pt 1.

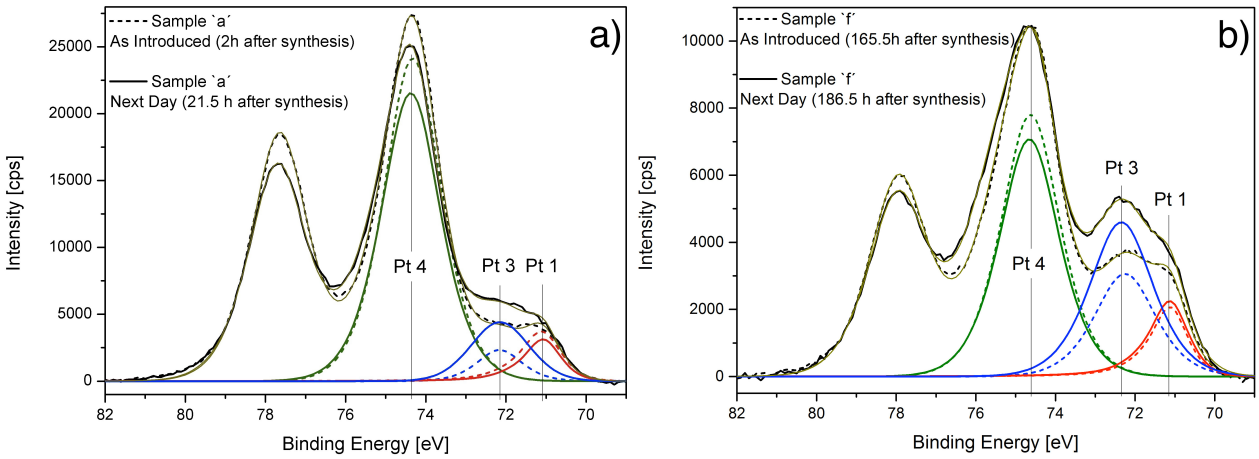

FIGURE 7. Time resolved degradation of $PtO_x(OH)_y(H_2O)_z$. a) shows the sample 'a' immediately after synthesis and after approximately 20 h in vacuum. b) shows the sample 'f' 165.5h hours after synthesis (in air) and after approximately 20 additional hours in vacuum. No peak normalization was performed.

The [Pt 3]/[Pt 4], [Pt 1]/[Pt 4] and [Pt]/[O] values for all samples ('a' through 'g') are found in fig. 8. The times shown for the bars labeled "As Introduced" are correct while the "Next Day" bars are offset from the former by only two hours for clarity. The "Next

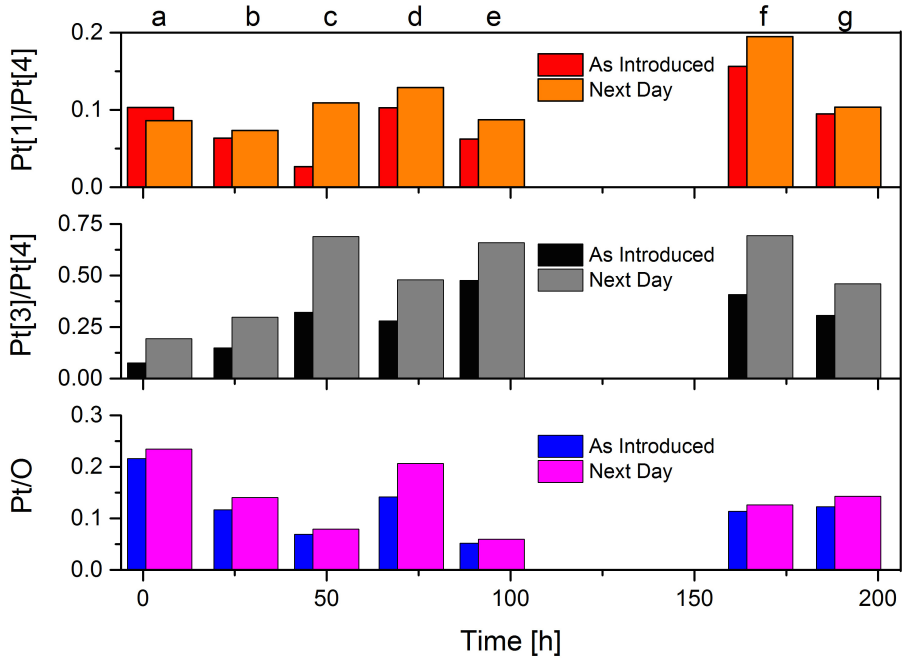

FIGURE 8. The [Pt 3]/[Pt 4], [Pt 1]/[Pt 4] and [Pt]/[O] ratios of the samples 'a' through 'g' are displayed both immediately after introduction into the vacuum chamber and after subsequent measurements the next day (samples remained in vacuum for approx. 24 hours despite the smaller x-position shift of "Next Day" bars). The increase in the [Pt 3]/[Pt 4] ratio is evident and is larger than the increase in the [Pt 1]/[Pt 4] ratio over the entire duration. The different degradation rates on the sample surface indicate the presence of intermediates states with differing finite stability.

Day" measurements were actually performed after differing times in vacuum (approx. 24 h after the corresponding "As Introduced" time). The large spread in values evident in the graphical plot attests to the large lateral film variation occurring during film synthesis and the differing states of degradation present on the $\sim$1 cm^2 samples as well as locally differing, finite degradation rates. This important result shows that the intermediate states (also seen in fig. 4) through which the sample passes during degradation have finite stability. If the intermediate states were transient, one would expect to see a homogeneous decay across all samples. Thus, it becomes possible in further experiments to identify meta-stable intermediate thermodynamic states, for example specific $[Pt_i]/[Pt_j]$ and $[Pt_i]/[O]$ ratios (i, j=1, 3, 4), with the hope of stabilizing them for use as durable catalysts.

The trend toward degradation of Pt 4 to mainly Pt 3 in fig. 8 is clear in every sample while the value of [Pt 1]/[Pt 4] increases much less. After 212 h the $PtO_x(OH)_y(H_2O)_z$ film

still had not degraded to Pt 1, indicating the stability of the Pt 3 phase relative to the Pt 4 phase, a result also seen in the heating series. The main degradation pathway here is Pt 4 $\rightarrow$ Pt 3 and leaves the Pt 3 system in a meta-stable state. Apart from these, other pathways are also possible.

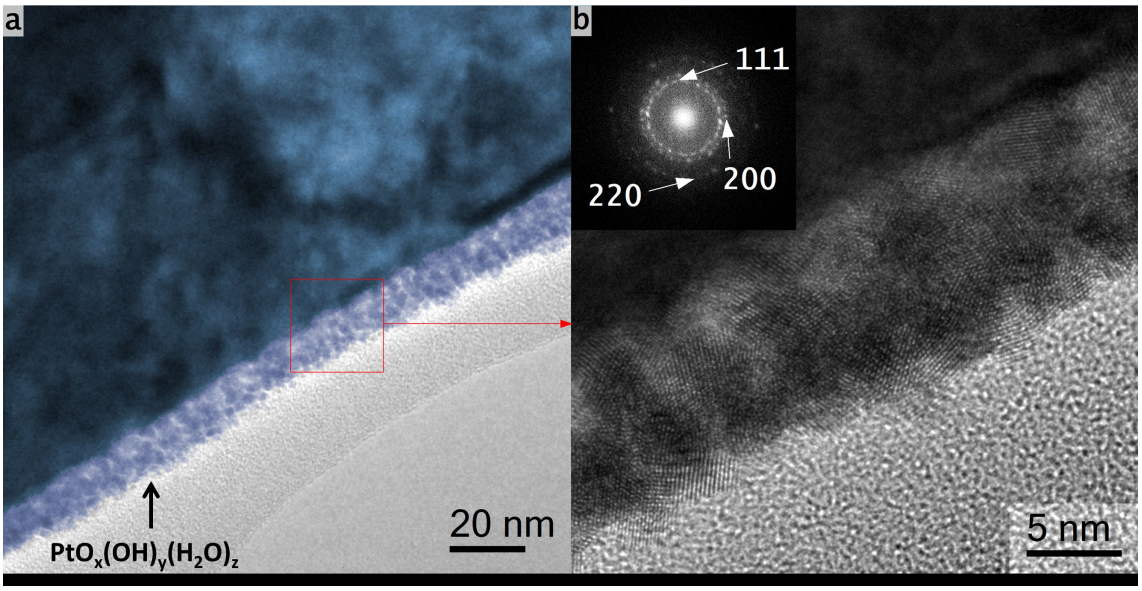

FIGURE 9. a) TEM image showing the $PtO_x(OH)_y(H_2O)_z$ film after the onset of degradation results in spheres (light blue in a)) on the sample surface with a Pt 1 (metal) core and hydrous oxide outer shell. b) shows a close-up of a region like that marked by the red box. Note: this is not the same sample on which the XPS studies were performed.

The degradation process was also studied with depth-profiling. The TEM image in fig. 9 a), with higher magnification of a region like that marked by the red box in b), shows the degradation of the anodized Pt films results in the formation of spheres of $PtO_x(OH)_y(H_2O)_z$ on the sample surface (central light blue layer in fig. 9 a)).[1] Energy dependent depth profiling at the KMC-1 beamline at the BESSY II synchrotron (Berlin, Germany) with the HIKE (HIgh Kinetic Energy) end station and angle resolved laboratory XPS measurements where used to study the make-up of the spheres. The fit regime is the same used in fig. 1 b).

Fig. 10 shows the results of the HIKE depth-profiling measurements in a) spectrum and b) numerical form with the increase in both the [Pt 1]/[Pt 4] and [Pt 3]/[Pt 4] ratios clearly

[1]The XPS studies were performed on different samples. The TEM images are only for illustrative purposes.

seen with increasing excitation energy. Here the atomic [Pt]/[O] ratios are also included in fig. 10 b) and can be divided into three regions marked by straight lines.

As a reference for the HIKE results, we repeated the measurement at 2500 eV excitation energy at the end of the experiment. Because the film degrades quickly in vacuum, a test was needed to determine whether the changes seen in the high energy measurements (performed after those at lower excitation energies) were due to the film's degradation or to the higher information depth. Fig. 10 c) shows the Pt 4f signal at 2500 eV at the beginning (labeled "Start" in fig. 10 c)) of the depth profiling and the reference measurement performed at the end (labeled "End" in figs. 10 b) and c)). The Pt 3 component in the "End" measurement is larger than that of the metal, which is typical of degradation (see the trend in fig. 7), while the high energy measurements have a larger metal component. Regarding beam damage (see discussion at the beginning of this section), we expect less here than in the laboratory measurements: at the high energies used at the HIKE beam line, the X-ray absorption cross sections are 1 to 2 orders of magnitude smaller than at surface sensitive energies (∼500 eV). Thus, although degradation during depth profiling is present, some of the increase in the metal signal must derive from the higher information depth.

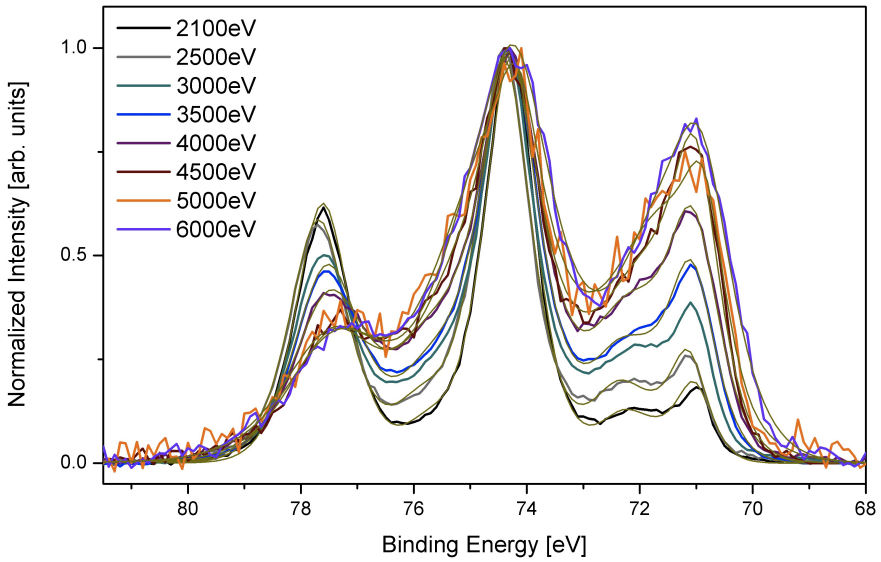

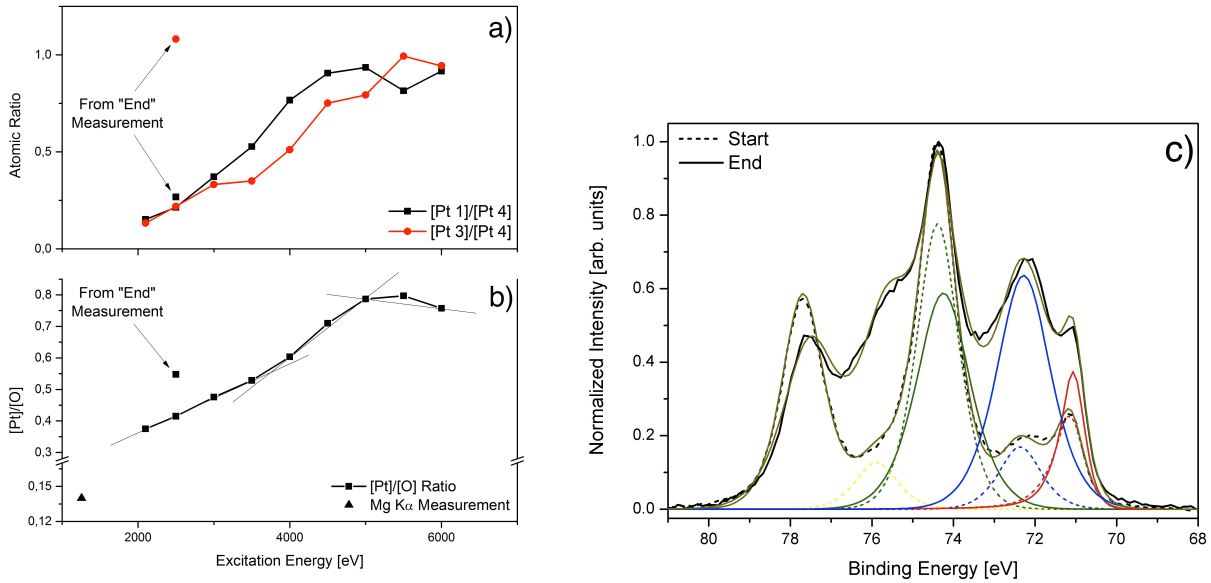

FIGURE 10. a) and b) depth profiling of the $PtO_x(OH)_y(H_2O)_z$ film showing an increase of the Pt 1 (metal) and Pt 3 signals with increased bulk sensitivity and atomic [Pt]/[O] ratios. c) the initial measurement at 2500 eV (labeled "Start") was repeated at the end (labeled "End") of the experiment to verify that the observed changes were due to the change in excitation energy (information depth) and not only sample degradation.

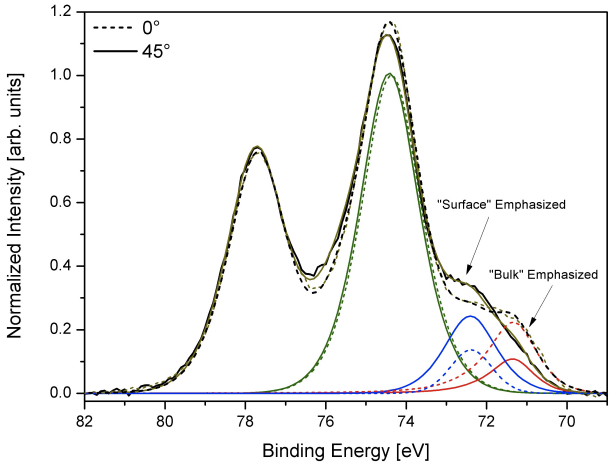

FIGURE 11. Angle resolved XPS measurement also showing an increase in the metal signal with increased bulk sensitivity.

Parallel to the HIKE measurements, angle resolved laboratory XPS measurements were used to investigate stoichiometric changes with depth. The spheres on the sample surface in fig. 9 are 5-7 nm in diameter so that with Al Kα radiation a signal variation with angle may be expected. The results in fig. 11 show, as with the HIKE measurements, an increase

in Pt 1 signal with depth. However, here, the [Pt 3]/[Pt 4] decreases with depth in contrast to the HIKE measurements.

Considering both the HIKE and angle resolved measurements, the spheres have a Pt 1 (metal) core and Pt 4 outer shell, although the exact position of Pt 3 in the structure remains ambiguous. Mixed between the core and outer shell, the Pt 3 phase may appear differently in experiments on different samples or at different points during sample degradation. Such a scenario describes the oxygen species leaving the center of the sphere, which is oxygen-depleted (metal), and diffusing outward, replenishing the oxygen that has already left the surface layers of the sphere. The three regions in the [Pt]/[O] ratio in fig. 10 b) are also consistent with a structure having a metallic core. Up to about 3500 eV the photoelectron signal penetrates deeper into the depth of the spheres shown in fig. 9 resulting in an increasing signal from the metal cores. After 5500 eV the signal begins to saturate and decline as higher excitation energies begin to penetrate the outer shells of the next layer of spheres. The first region indicates a nanoparticles size of ∼7 nm [40], slightly larger than the ∼5 nm radius seen in fig. 9. Finally, the inclusion of the [Pt]/[O] ratio from the Mg Kα measurement in fig. 10 b) shows the outer most layer contains a high amount of oxygen with a jump in the first several nm to a more Pt-rich composition. Thus, the outer termination layer may be almost completely devoid of platinum. Here we emphasize again the complexity of our surface morphology compared to more ordered surfaces, for example in [22], which necessitates the considerations for our fit regime.

5. $IrO_x(OH)_y(H_2O)_z$

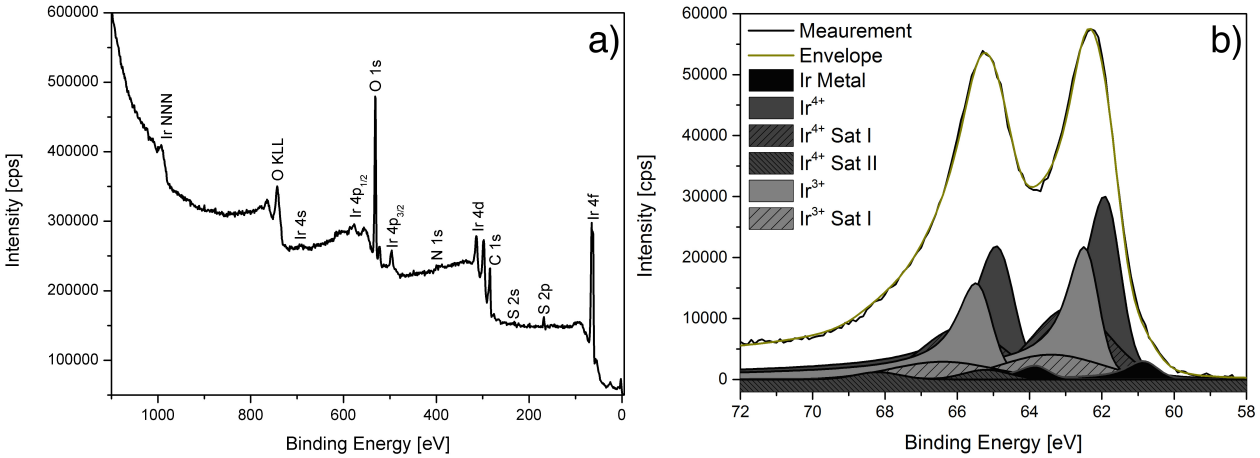

FIGURE 12. a) Typical XP survey spectrum of $IrO_x(OH)_y(H_2O)_z$ showing the constituent elements of Ir, O, S and N. b) typical detail of Ir 4f with Mg Kα radiation and the fit regime developed in [16, 17].

Fig. 12 a) shows a typical XP survey spectrum of the $IrO_x(OH)_y(H_2O)_z$ bulk hydrous oxide film.[2] Ir and O lines are evident along with N and S signals similar to those found in the $PtO_x(OH)_y(H_2O)_z$ films. b) shows a detail of the Ir 4f line measured with Mg Kα and fitted with Ir metal, Ir^{3+} and Ir^{4+} peaks along with the corresponding shake up peaks as described in [16, 17]. Here we draw attention to the lower oxidation state Ir^{3+}, which, in contrast to platinum oxide, has a higher binding energy than the higher oxidation state Ir^{4+}. The fitted peaks were allowed to vary slightly in binding energy compared to [16, 17] to achieve a quality fit; a difference may be expected because these samples have a different (hydrous) structure compared to the samples in the prior study. Also in contrast to $PtO_x(OH)_y(H_2O)_z$, the $IrO_x(OH)_y(H_2O)_z$ films exhibit no observed change in the XP spectra over time: the metal contribution to the spectrum is stable and results from thin regions in the layer. A preliminary fit of the O 1s peak (without corrections for carbon-oxygen bonds) resulted in a stoichiometry of $IrO_{0.4}(OH)_{2.3}(H_2O)_1$

The $IrO_x(OH)_y(H_2O)_z$ layer was investigated at BESSY II on the KMC-1 beamline with the HIKE end station. The results are shown in fig. 13 in both a) spectrum and b) numerical

[2]The use of the indices x, y and z does not indicate a connection to the stoichiometry of the $PtO_x(OH)_y(H_2O)_z$ samples. These common letters are used here only for convenience.

TABLE 4. Parameters for the Ir 4f XPS fits. The line shape (DS = Doniach-Sunjic) in pro cent Gauss (G) and Lorentz (L), binding energy (B.E.) of the Ir $4f_{7/2}$ component, full width at half maximum (the same for the Ir $4f_{7/2}$ and Ir $4f_{5/2}$ components) and peak separation, ΔE, between 7/2 and 5/2 components are given.

	Ir Metal	Ir^{3+}	Ir^{3+} Sat I	Ir^{4+}	Ir^{4+} Sat I
Line Shape	DS, 60% G, 40% L	DS, 60% G, 40% L	0% G, 100% L	DS, 60% G, 40%L	0% G, 100% L
B.E. ($4f_{7/2}$)	60.90 eV	62.55 eV	63.4 eV	62.00	62.85 eV
FWHM	0.95 eV	0.95 eV	3.20 eV	1.05 eV	2.47 eV
ΔE	3.00 eV	3.00 eV	3.00 eV	3.00 eV	3.00 eV

form.

A decrease in the $[Ir^{3+}]/[Ir^{4+}]$ ratio with depth is evident and correlates with the increasing total [Ir]/[O] ratio shown at the bottom of the figure. The Ir^{3+} state is associated with a defect structure in the $IrO_x(OH)_y(H_2O)_z$ film [16, 17] and will have a higher density at lower Ir concentrations on the sample surface; the density will decrease as less oxygen allows a trend toward more stoichiometric IrO_2 deeper in the sample. As in fig. 12, the HIKE sample has thin regions causing a metal signal in the high kinetic energy XP spectra that increases with excitation energy, shown in the $[Metal]/[Ir^{4+}]$ ratio. Here the ratio from the Mg Kα measurement has been added for comparison. In order to illustrate the large dependence of the Ir 4f fit on binding energy, the HIKE data was fitted in three regimes. The Ir 4f binding energy was calibrated using the Pt 4f metal peak with the calculated ratios found in the middle $[Ir^{3+}]/[Ir^{4+}]$ curve (fig. 13, "At Calib. Energy"). Moving the peaks 0.1 eV to either higher or lower binding energy produces drastic changes in the $[Ir^{3+}]/[Ir^{4+}]$ ratio, especially at low excitation energies. However, the trend in the $[Ir^{3+}]/[Ir^{4+}]$ ratio remains the same no matter the fit regime. For this reason, we lay importance on the qualitative behavior of the $[Ir^{3+}]/[Ir^{4+}]$ ratio with depth.

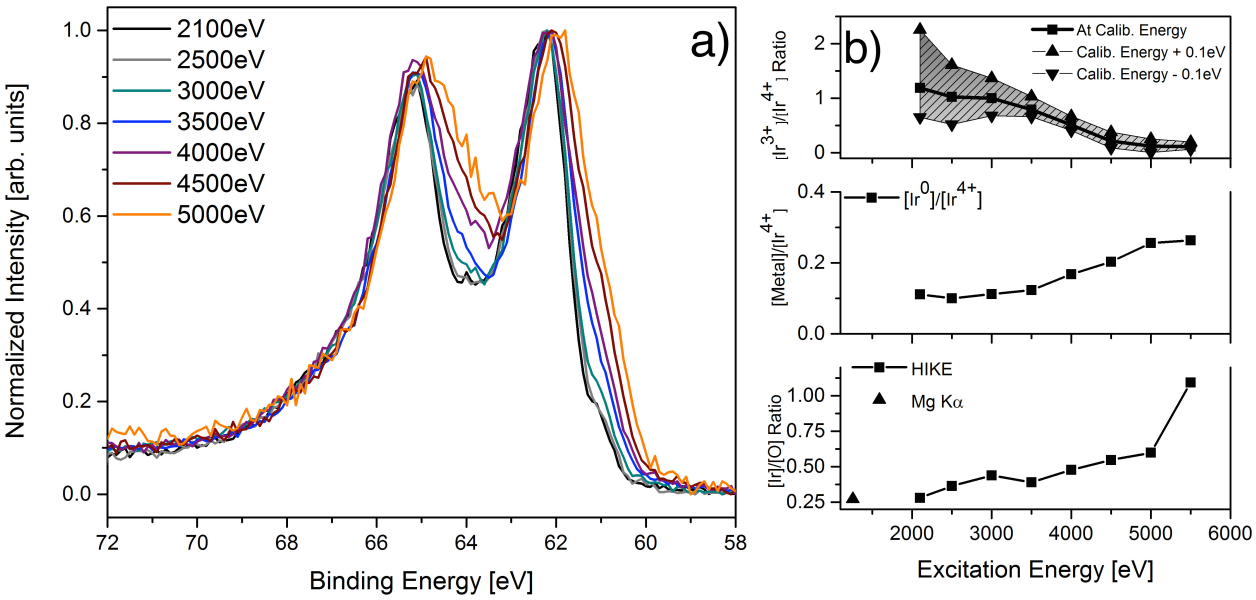

FIGURE 13. a) and b) depth profiling of the $IrO_x(OH)_y(H_2O)_z$ film. An increase of the Ir^{4+} species and [Ir]/[O] ratios are evident with increased information depth.

Initial heating experiments to approximately 200°C for 30 sec (not shown) reduced the contribution of the Ir^{3+} to the Ir 4f spectrum. This supports the model of the Ir^{3+} proposed in [16, 17] because heating leads to a reduction of defect density and emphasizes the samples are not composed of a stoichiometric IrO_2 phase as this remains stable in vacuum up to ~570°C [42].

6. Chemical Discussion

The spectroscopic observations on the Pt electrode merit some chemical interpretation as despite the well-known "fact" that Pt oxidizes [43, 44] in OER conditions it is not easily reconciled with the nobility of metallic Pt. In fig. 14 we have compiled the oxidation chemistry of Pt using both gas phase oxygen and electrochemical oxidation.

Pt metal in pure form is highly resistant to gas phase oxidation and can even be melted in air without oxide formation. At elevated pressures above 8 bar a sub-surface oxide forms allowing the production of PtO at 1023 K. Only under high oxygen pressure combined with

alkali oxide melts (or alkali peroxide-hydroxide melts) can higher valent Pt oxo-salts be obtained.

Pure PtO_2 cannot be obtained by gas phase oxidation. Only a combination of electrochemical oxidation followed by calcination at 673 K to remove hydroxides will lead to PtO_2 that decomposes in mixed-valent orthoplatinic and metaplatinic acids. And these products eventually decompose in nanostructured Pt metal known as Pt black. The electrochemical oxidation products also tend to decompose at 300 K into Pt black with a half-life of about a day.

Hexavalent PtO_3 can only be obtained as a poorly defined product at high oxidation potentials in alkaline electrolytes from where it can easily decompose the alkali salts from the orthoplatinic acid.

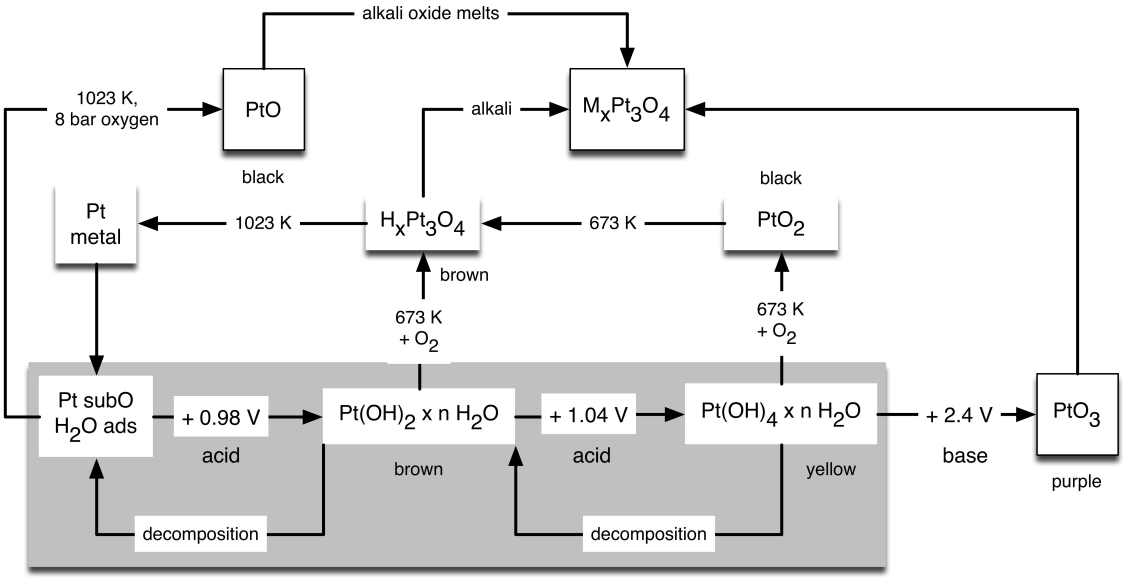

FIGURE 14. Scheme of oxidation pathways and prominent products of platinum metal. The shaded reactions occur during OER.

It is evident in the scheme in fig. 14 that under electrochemical conditions relevant for the present study we can expect mixtures of metallic and orthometallic forms of platinic

acid in tetravalent and divalent forms. Such species can also be seen as oligomers of hydrated Pt hydroxo-complexes. The extent of poly-condensation will depend on ion strength, pH, temperature and time of reaction and may thus have poor reproducibility. The high thermal reactivity found in the spectroscopic experiments is a direct consequence of the still oligomeric form of the compounds allowing further facile condensation upon thermal removal of aquoligands. It is expected further that different attempts to characterize the termination layer of a Pt electrode under OER, or post-OER, will lead to differing structures as a likely different extent of condensation and cross-linking will be obtained.

The presence of aquo, hydroxo, and oxo-ligands on Pt ions of divalent and possibly tetravalent oxidation states will further allow for the coordination of hydro-peroxo species, $-OOH$, as terminal ligands. It is instructive to recall the properties of coordination compounds with this particular ligand [45, 46, 47, 48]. The high propensity of both divalent [48] and tetravalent Pt to form hydrido-complexes is reflected in the reactivity of hydro-peroxo complexes that easily release di-oxygen. The formation of this ligand can thus be considered an insertion reaction of di-oxygen into a Pt-H bond [46]. Such reactions can also be induced by photo-elimination [49], implying that a radicalic rather than a homolytic mechanism is responsible for insertion/elimination. In all cases Pt-OH co-ligands play important roles as hydrogen donors and/or hydrogen bridge stabilizers. It is likely, therefore, that such reaction pathways are also active in the OER considering the multi-hydroxylated environment of Pt ions. The fact that they may still be in contact with the metallic substrate (for current flow) and that they exist in an electron-rich environment during OER renders the comparison with the coordination compounds carrying electron-donating nitrogen ligands even more plausible.

Similar considerations may be made for the Ir hydrous oxides. Studies on molecular Ir coordination chemistry about the formation of oxidation catalysts in water in the presence of an inorganic oxygen donor show that $NaIO_3$ can be considered equivalent to a peroxo species in solution [50, 51]. Deposition of such complexes on ITO electrodes led, in fact, to the formation of active OER electrodes, albeit with limited stability [52]. This behavior is well understandable in the light of the condensation chemistry of Ir in the presence of

di-oxygen. Using a combination of UV-spectroscopy and EPR it was shown that in (basic) aqueous solution a mixture of species, indicated in fig. 15, should co-exist and slowly interconvert at ambient temperature [53]. It is conceivable that such species would rapidly interconvert at elevated temperatures into poorly ordered polymeric forms of "IrO_2" with residual peroxo-species, as shown in the present study.

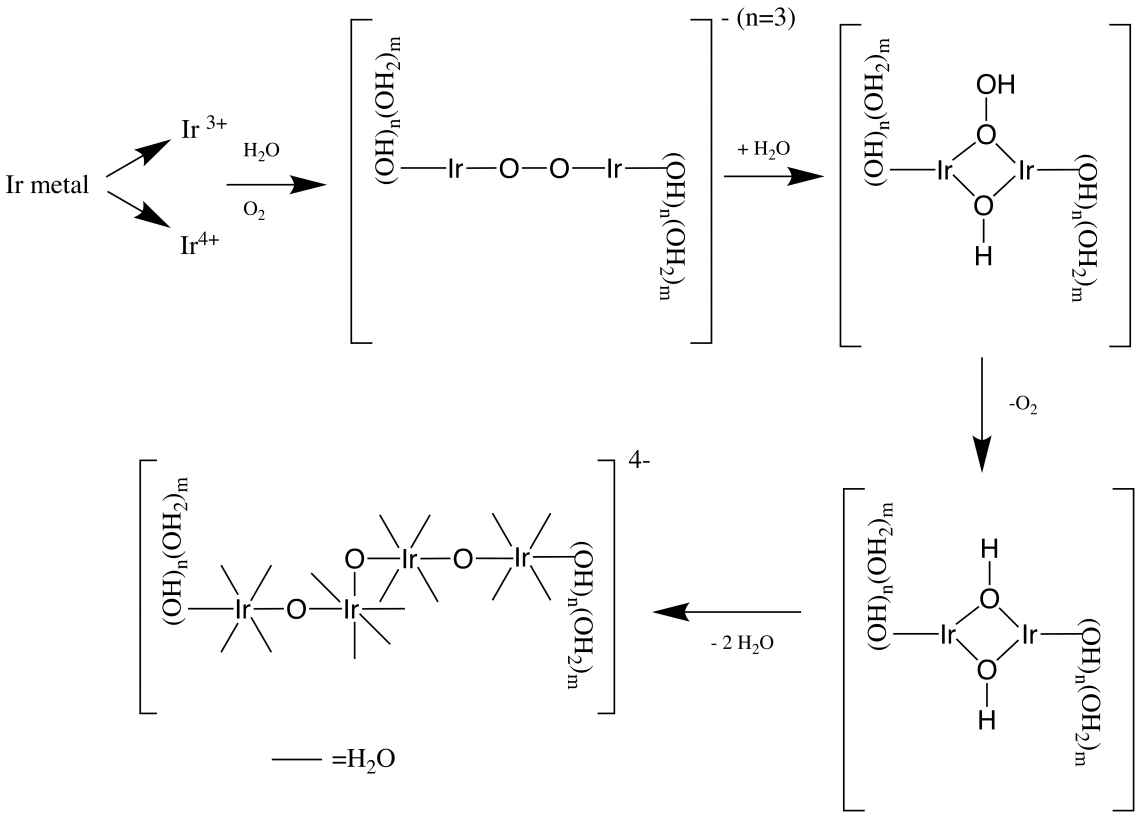

FIGURE 15. A small section of the condensation chemistry of Ir under OER conditions. The electrode corrodes into a mixture of Ir^{3+} and Ir^{4+} that are both stable in water. In the presence of di-oxygen and water the redox chemistry involving condensation of both valences followed by an oxidation of Ir, formation of hydrogen and under elimination of di-oxygen, leads to a di-hydroxo complex. This complex undergoes poly-condensation into poorly ordered Ir oxide with residual hydroxo and peroxo ligands. Only calcination will transform this solid into genuine IrO2 (see comment on heat treatment at the end of section 5).

More work is needed to elucidate the exact nature of the polycondensation and polymerization chemistry that is much richer in the case of Ir than in the case of Pt due to the facile coordination of di-oxygen on Ir^{3+} species being a meta-stable form of Ir in aqueous solution. In the case of Pt perhaps the high propensity of metal-hydrido bonds gives rise to a different

sequence of events in water activation than in the case of the highly oxophilic Ir species.

7. Conclusion

Pt and Ir metal foils were oxidized through anodization resulting in complex Pt and Ir hydrous oxide layers. XPS measurements were similar to those found in the literature in the prior four decades, however, here we emphasize that the spectra contain no direct information about the phases present in the films and real information about short or long-range order must be gathered from other experiments or theoretically.

Although both samples are based on noble metals, the resulting anodized layers differed in several respects.

The $PtO_x(OH)_y(H_2O)_z$ layer degraded after synthesis forming surface core-shell structures with a metal core and Pt 4 outer shell, the termination layer of which contains almost no Pt. The degradation process was different depending on whether the sample was heated (Pt 4 $\rightarrow$ Pt 3 $\rightarrow$ Pt 1 pathway) or left to degrade in air (Pt 4 $\rightarrow$ Pt 3 pathway). The low heat needed to accelerate degradation indicates the absence of any actual extended regions of stable, stoichiometric PtO or PtO_2 phases. Also, samples made simultaneously on a single piece of foil had large lateral variations in composition. This points to the existence of non-transient intermediate states with finite lifetimes.

In comparison, the $IrO_x(OH)_y(H_2O)_z$ films were stable over time. Depth profiling showed the layers to be oxygen rich on the surface with a high Ir^{3+} density. The Ir^{4+} density increased with depth along with the Ir content indicating a more ordered material nearer the substrate. Heating further decreased the Ir^{3+} density and supports the creation of the oxidation state through defects.

Future experiments will expand on this work by concentrating on measurements more sensitive to physical surface structure and chemical environment (EXAFS, NEXAFS) to

identify the intermediate thermodynamic states seen during degradation (fig. 4). In order to successfully identify suitable catalytic layers, materials science must understand the complex kinetics of degradation in order to stabilize these intermediate states. Differences seen *in-* and *ex-situ* as well as between samples exposed to air and those kept in anaerobic environments before being loaded into the vacuum chamber will enable conclusions to be drawn about catalysts in active states and the effects of different measurements methods on a system. The importance of this step is underlined by the often *ex-situ* nature of the spectroscopic methods used in this study. These data will build a strong foundation for future experiments at the EMIL beamline at BESSY II in Berlin.

Acknowledgements: We thank the Helmholtz-Zentrum-Berlin (Electron Storage Ring BESSY II) for providing synchrotron radiation at the KMC-1 beam line.

References

[1] D. G. Nocera, Acc. Chem. Res., **45**, 767-776 (2011)

[2] H. Kasai, H. S. Nalwa, H. Oikawa, S. Okada, H. Matsuda, N. Minami, A. Kakuta, K. Ono, A. Mukoh, H. Nakanishi, Jpn. J. Appl. Phys., **31**, L 1132-L 1134 (1992)

[3] B. C. Sales, J. E. Turner, M. B. Maple, Surface Science **114** 381-394 (1982)

[4] M. T. M. Koper, W. Schmickler, Cehm Phys. **211** 123-133 (1996)

[5] M. T. M. Koper, A. P. J. Jansen, R. A. van Santen, J. J. Lukkien, P. A. J. Hilbers, J. Chem. Phys. **109** 6051-6062 (1998)

[6] H. Yamazaki, A. Shouji, M. Kajita, M. Yagi, Coord. Chem. Rev., **254**, 2483-249 (2010)

[7] M. W. Kanan, D. G. Nocera, Science, **321**, 1072-1075 (2008)

[8] H. J. M. Hou, Journal of Integrative Plant Biology, **52**, 704-711 (2010)

[9] H. Dau, C. Limberg, T. Reier, M. Risch, S. Roggan, P. Strasser, ChemCatChem, **2**, 724-761 (2010)

[10] N. Lewis, D. G. Nocera, P. Natl. Acad. Sci. USA **103**, 15729-15735 (2006)

[11] R. Schlögl, ChemSusChem , **3**, 209-222 (2010)

[12] N. I. Shutilova, D. N. Moiseev, Prot. Met. Phys. Chem. Surf., **46**, 502-507 (2010)

[13] J.-Y. Chung, F. Aksoy, M. E. Grass, H. Kondoh, P Ross, Jr., Z Liu, B. S. Mun, Surf. Sci. Lett., **603** L35-L38 (2009)

[14] N. Alonso-Vante, B. Schubert, H. Tributsch, Mat. Chem. Phys., **22**, 281-307 (1989)

[15] R. Arrigo, M. Hävecker, M. E. Schuster, C. Ranjan, E. Stotz, A. Knop-Gericke, R. Schlögl, Ang. Chem., **125** 11874-11879 (2013)

[16] V. Pfeifer, T.E. Jones, J.J. Velasco Vélez, C. Massué, Rosa Arrigo, D. Teschner, F. Girgsdies, M. Scherzer, M.T. Greiner, J. Allan, M. Hashagen, G. Weinberg, S. Piccin, M. Hävecker, A. Knop-Gericke, R. Schlögl, Surf. Int. Ana., DOI: 10.1002/sia.5895 (2015)

[17] V. Pfeifer, T.E. Jones, J.J. Velasco Vélez, C. Massué, M.T. Greiner, Rosa Arrigo, D. Teschner, F. Girgsdies, M. Scherzer, J. Allan, M. Hashagen, G. Weinberg, S. Piccin, M. Hävecker, A. Knop-Gericke, R. Schlögl, Phys. Chem. Chem. Phys., **18** 2292-2296 (2016)

[18] C. Ranjan, R. Arrigo, M. E. Schuster, R. Schlögl, M. Eiswirth, B. Johnson, F. Girgsdies, G. Weinberg, A. Knop-Gericke, J. Tornow, Some Journal **Vol.** 0000-9999 (2014)

[19] M. Gorgoi, S. Svensson, F. Schäfers, W. Braun, W. Eberhardt, Eur. Phys. J. Special Topics, **169**, 221-225 (2009)

[20] J. J. Yeh, I. Lindau, Atomic Data and Nuclear Data Tables, **32**, 1-155 (1985)

[21] M.B. Trzhaskovskaya, V.I. Nefedov, V.G. Yarzhemsky, Atomic Data and Nuclear Tables **77**, 97-159 (2001)

[22] D. R. Butcher, M. E. Grass, Z. Zeng, F. Aksoy, H. Bluhm, W.-X. Li, B. Mun, G. A. Somorjai, Z. Liu, JACS, **133** 20319-20325 (2001)

[23] H. Junge, N. Marquet, A. Kammer, S. Denurra, M. Bauer, S. Wohlrab, F. Gärtner, M.-M. Pohl, A. Spannenberg, S. Gladiali, M. Beller, Chem. Eur. J., **18** 12749-12758 (2012)

[24] C.T. Au, M.W. Roberts, Chem. Phys. Lett. **74**, 472-474 (1980)

[25] M.W. Roberts, Pure & Appl. Chem., **53**, 2269-2281 (1981)

[26] I.M., Kodintsev, S. Trasatti, M. Rubel, A. Wieckowski, N. Kaufher, Langmuir, **8**, 283-290 (1992)

[27] W.N. Delgass , T.R. Hughes, C.S.Fadley, Cat. Rev.: Sci Eng., **4**, 179-220 (1971)

[28] K.S. Kim, N. Winograd, R.E. Davis, J. Am. Chem. Soc., **93**, 6296-6297 (1971)

[29] G.C. Allen, P.M. Tucker, A. Capon, R. Parsons, Electroanal. Chem. Inter. Electrochem., **50** 335-343 (1974)

[30] J.S. Hammond, N. Winograd, J. Electroanal. Chem., **78** 55-69 (1977)

[31] M. Salmerón, L. Brewer, G.A. Somorjai, Surface Science **112** 207-228 (1981)

[32] M. Peuckert, H.P. Bonzel, Surface Science Lett., **145** A372 (1984)

[33] M. Peuckert, Surface Science, **144** 451-464 (1984)

[34] J.B. Goodenough, A. Hamnett, B.J. Kennedy, R. Manohran, S.S. Weeks, J. Electroanal. Chem., **240** 133-145 (1984)

[35] L. Atanasoska, R. Atanasoski, S. Trasatti, Vacuum, **40**, 91-94 (1990)

[36] G. Lalande, M. C. Denis, D. Guay, J.P. Dodelet, R. Schulz, J. Alloys and Comp., **292** 301-310 (1999)

[37] B. Yang, Q. Lu, Y. Wang, L. Zhuang, J. Lu, P. Liu, Chem. Mater., **15** 3552-3557 (2003)

[38] S. Axnanda, E.J. Crumlin, B. Mao, S. Rani, R. Chang, P. Karlsson, M.O.M. Edwards, M. Lundqvist, R. Moberg, P. Ross, Z. Hussain, Z. Liu, Sci. Rep., **5** 9788 (2015)

[39] N. Smith, G. K. Wertheim, S. Hüfner, M. M. Traum, Phys. Rev. B, **10**, 3197-3206 (1974)

[40] S. Tanuma, C. J. Powell, D. R. Penn, Surf. Interf. Anal. **21** 165 (1994)

[41] L. K. Ono, J. R. Croy, H. Heinrich, B. Roldan Cuenya, J. Phys. Chem. C, **115** 16856-16866 (2011)

[42] E. H. P. Cordfunke, Thermochimica Acta, **50** 177-185 (1981)

[43] J.O. Bockris, A. Huq, Proc. Royal Soc. London, Series A, Math. Phys. Sci., **237** 277-296 (1956)

[44] A. Damjanovic, V.I. Birss, D.S. Boudreaux, J. Electrochem. Soc., **138** 2549-2555 (1991)

[45] A.V. Sberegaeva, W.-G. Liu, R.J. Nielsen, W.A. Goddard, III, A.N. Vedernikov, J. Am. Chem. Soc., **136** 4761-4768 (2014)

[46] D.D. Wick, K.I. Goldberg, J. Am. Chem. Soc., **121** 11900-11901 (1999).

[47] P. Fantucci, S. Lolli, M. Pizzotti, R. Ugo, Inorg. Chim. Acta, **270** (1998) 479-487.

[48] R.A. Michelin, R. Ros, G. Strukul, Inorg. Chim. Acta, **37** L491-L492 (1979)

[49] L.A. Wickramasinghe, P.R. Sharp, J. Am. Chem. Soc., **136** 13979-13982 (2014)

[50] U. Hintermair, S.W. Sheehan, A.R. Parent, D.H. Ess, D.T. Richens, P.H. Vaccaro, G.W. Brudvig, R.H. Crabtree, J. Am. Chem. Soc., **135** 10837-10851 (2013)

[51] W.J. Tenn, III, K.J.H. Young, J. Oxgaard, R.J. Nielsen, W.A. Goddard, III, R.A. Periana, Organometallics, **25** 5173-5175 (2006)

[52] J.D. Blakemore, N.D. Schley, G.W. Olack, C.D. Incarvito, G.W. Brudvig, R.H. Crabtree, Chem. Sci., **2** 94-98 (2011)

[53] L.I. Kuznetsova, S.V. Koscheev, N.I. Kuznetsova, L.G. Detusheva, React. Kin. Mech. Cat., **101** 1-12 (2010)